Soft Matter

PAPER

View Article Online
View Journal | View Issue

Cite this: *Soft Matter*, 2023, **19**, 5622

Re-entrant transitions of locally stiff RNA chains in the presence of polycations leads to gelated architectures

Isha Malhotra and Davit A Potoyan *

Received 13th March 2023,
Accepted 22nd June 2023

DOI: 10.1039/d3sm00320e

rsc.li/soft-matter-journal

The liquid–liquid phase separation of protein and nucleic acid mixtures drives the formation of numerous membraneless compartments in cells. Temperature variation is commonly used for mapping condensate phase diagrams, which often display unique upper critical temperatures. Recent report on peptide–RNA mixtures has shown the existence of lower and upper critical solution temperatures, highlighting the importance of temperature-dependent solvent and ion-mediated forces. In the present work, we employ residue-level coarse-grained models of RNA and polycation peptide chains for simulating temperature-induced re-entrant transitions and shedding light on the role played by mobile ions, temperature-dependent dielectric permittivity, and local chain stiffness. We show that differences in bending rigidity can significantly modulate condensate topology leading to the formation of gelated or fibril like architectures. The study also finds that temperature dependence of water permittivity is generally sufficient for recapitulating experimentally observed closed loop and LCST phase diagrams of highly charged protein–RNA mixtures. However, we find that similar-looking closed-loop phase diagrams can correspond to vastly different condensate topologies.

The liquid–liquid phase separation (LLPS) of biomolecules is implicated in the biogenesis and regulation of numerous membraneless cellular bodies.[1–7] Prominent examples of membraneless bodies formed *via* biomolecular phase-separation include nucleolus,[8,9] stress granules,[10,11] chromatin domains and ribonucleoprotein (RNP) bodies.[12,13] Taking inspiration from biology, the mechanism of LLPS is also widely used for bio-engineering applications, including elastin generation in vertebrate tissues[6] and for creating adhesives from sand-castle worms.[14]

To learn the driving forces of phase separation in biomolecular mixtures, *in vitro* experiments use variable conditions to map condensate phase diagrams.[15–17] Temperature and salt variation are commonly adopted for quantifying coexistence windows of peptide and nucleotide mixtures.[18–20] For many protein and nucleic acid mixtures, one often finds a single well-defined upper critical temperature which indicates the dominance of energetic contacts in determining thermodynamic stability. Indeed a large number of experimental[6,18,19,21–28] and computational studies[29–36] show that an interplay of sequence charge and hydrophobic patterns is sufficient for explaining and characterizing thermodynamics and material properties of a wide range of protein condensates. A significant recent effort has therefore been directed to refining the residue level physics-based coarse-grained models predicting single chain and condensed phase behavior of proteins with near quantitative accuracy.[37–41]

Unsurprisingly the role of forces other than direct biomacromolecular associative interactions, such as the effect of temperature on the dielectric constant, solvent reorganization, ion correlation, and variable conformational flexibility of chains, has remained a relatively less explored aspect of biomolecular LLPS.[42,43] In this respect, the protein–RNA mixtures with low complexity RNA and protein sequences have become a convenient model system for studying the interplay of direct associative interactions and ion/solvent-mediated forces because these mixtures display a wide range of complex thermodynamic phase diagrams and condensate morphologies.[18–20,44–46] In a recent report, Alsharedah *et al.*[19] have shown the existence of LCST and closed-loop phase diagrams in RNA and polycation mixtures, which suggested the critical roles of ion-meditated interactions.

In the present study, we employ residue resolution coarse-grained models of proteins and RNA chains with implicit and explicit ions to systematically explore temperature-induced re-entrant phase-transitions in RNA–polycation mixtures.[19] Simulations show that the temperature dependence of the aqueous dielectric constant is sufficient for recapitulating LCST. By studying both explicit and implicit electrostatic models, we further establish that temperature-dependent dielectric constant modulates charge correlations in the system, thereby controlling the coexistence window of LCST. We shed light on the role

Department of Chemistry, Iowa State University, Ames, Iowa 50014, USA.
E-mail: potoyan@iastate.edu

of chain stiffness by showing that varying chain stiffness can significantly affect condensate topology and material properties. Finally, we show that chain stiffness and strong electrostatic charge correlations can lead to gelated or fibril-like architectures with large characteristic length scales.

We note that a similar conclusion about the microscopic origin of LCST has already been reached in several recent studies of temperature-induced coacervation of polyelectrolyte mixtures[47,48] where temperature dependence of the dielectric constant was found sufficient to capture entropic forces such as solvent reorganization affecting hydrophobic and ionic interactions. The importance of the temperature-dependent dielectric constant is also seen when considering the Bjerrum length, which increases as a function of temperature, thereby creating stronger electrostatic correlations that drive phase separation at higher temperatures. Atomistic simulations of charged peptide mixtures[49] and disordered proteins[50] have also reported significant contributions of ion release and dissociation to free energy of coacervation.

1 Methods

We have employed the widely used[29,42] one bead per residue/base coarse-grained models for proteins and RNA chains (see Fig. 1). The energy function for the protein–RNA mixtures encodes short-range RNA–RNA, protein–protein and RNA–protein interactions, and long-range electrostatics. The energy function encoding intra- and inter-chain interaction of proteins and RNAs are as follows:

$$U = \sum_{\text{bonds}} U_{\text{bond}}(r_{ij}) + \sum_{i<j} \left[U_{\text{elec}}(r_{ij}) + U_{\text{nb}}(r_{ij})\right] \quad (1)$$

where U_{bond} is a harmonic spring

$$U_{\text{bond}}(r_{ij}) = k_{\text{spring}}(r - r_0)^2 \quad (2)$$

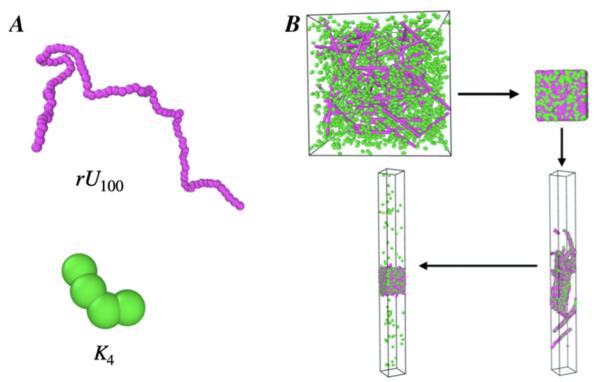

Fig. 1 (A) Shown are coarse-grained models used to study the phase equilibrium of protein–RNA mixtures with *PolyU*$_r$ RNA depicted by pink and K_4 in green color. (B) The simulation protocol following[51] is used for computing binodal from direct coexistence simulations of multiphase mixtures. Size variation has been done to ascertain the negligible effect of finite size effects. The system is set up in a uniformly mixed state and is gradually compressed subject to a temperature ramp. The box is then elongated along the direction z subject to cooling, forming a slab.

with a spring constant $k_{\text{spring}} = 8000$ and equilibrium bond length $r_0 = 0.38$ nm for proteins and $k_{\text{spring}} = 1000$ and $r_0 = 0.7$ nm for RNA. To account for the stiffness of RNA chains, we add angular harmonic term $k_\theta(\theta - \theta_0)^2$ is included where $k_\theta = 50.0$ and $\theta_0 = \pi$.

The non-bonded interactions are modeled by Lennard-Jones potential or by Ashbaugh-Hatch functional form (HPS)[52] (see Table 1).

$$U_{\text{nb}}(r_{ij}) = \begin{cases} U_{\text{LJ}}(r) \\ \text{or} \\ U_{\text{HPS}}(r) \end{cases} \quad (3)$$

Table 1 shows the different methods employed in the current study to implement the nonbonded interactions. (1) LJ potential, where residues' explicit temperature dependence and hydrophobicity are neglected. (2) HPS potential incorporates the temperature dependence of solvent-mediated interactions.

Ashbaugh–Hatch potential form is given as:

$$U_{\text{HPS}}(r) = \begin{cases} U_{\text{LJ}}(r) + (1-\lambda)\varepsilon & r \le 2^{\frac{1}{6}}\sigma \\ \lambda U_{\text{LJ}}(r) & \text{otherwise} \end{cases} \quad (4)$$

where $U_{\text{LJ}}(r)$ is the standard Lennard-Jones(LJ) potential shown below:

$$U_{\text{LJ}}(r) = 4\varepsilon_{ij}\left[\left(\frac{\sigma_{ij}}{r}\right)^{12} - \left(\frac{\sigma_{ij}}{r}\right)^{6}\right] \quad (5)$$

Here, $\sigma_{ij} = \frac{(\sigma_i + \sigma_j)}{2}$, where σ_i and σ_j are the van der Waals radius of residue i and j respectively. This form of the potential allows tuning the attractiveness of the interactions based on the parameter λ, which is adapted from the hydropathy scale proposed by Urry *et al.*[37,53] λ varies between 0 and 1, corresponding to the least and most hydrophobic residues. The pair potential for $\lambda = 0$ consists of only the repulsive part of the interaction corresponding to the Weeks–Chandler–Andersen functional form[54] and $\lambda = 1$ corresponds to the Lennard-Jones potential. When temperature dependence is included in $\varepsilon_{ij}(T)$, the interaction strength between residues i and j is given by $\lambda_{ij} = \frac{\lambda_{i,\text{HPS}} + \lambda_{j,\text{HPS}}}{2}$. The temperature dependence of solvent-mediated interactions can also be encapsulated by making

Table 1 Simulated systems. LJ and HPS represent the systems where nonbonded interactions are modeled through Lennard-Jones potential and Ashbaugh and Hatch functional form, respectively. DH and PPPM represent systems where electrostatic interactions are treated with Debye–Huckel and PPPM methods

Name	Bonded	Non-bonded	Electrostatic
LJ + DH	Harmonic	Lennard-Jones	Debye–Hückel
LJ + PPPM	Harmonic	Lennard Jones	PPPM
HPS + DH	Harmonic	HPS-Urry(T)	Debye–Hückel
HPS + PPPM	Harmonic	HPS-Urry(T)	PPPM
HPS($\varepsilon(T)$) + DH	Harmonic	HPS-Urry($\varepsilon(T)$)	Debye–Hückel
LJ	Harmonic	Lennard Jones	No electrostatics

short-range interactions temperature dependent *via* hydropathy parameter $\lambda_{ij}(T)$, which can provide further insight into the nature of hydrophobic *vs.* polar interactions. $\lambda_{ij}(T)$ is the temperature-dependent interaction strength between residues i and j and is given as $\lambda_{ij}(T) = \frac{\lambda_i(T) + \lambda_j(T)}{2}$. We find closer agreement with experiment when we consider K to be a hydrophobic residue[55] and rU an aromatic residue.[56] The lysine side chain contains four methylene, and they exhibit hydrophobic interactions if the charged ε–NH_3^+ group is hydrogen-bonded. We have adapted the equation for the temperature dependence of aromatic and hydrophobic residues from ref. 42. We have also investigated the system where all non-bonded residue pairs interact *via* the simple LJ potential.

$$\lambda_{i,A} = \lambda_{i,\mathrm{HPS}} - 26.189 + 0.15034T - 0.00020920T^2 \quad (6)$$

$$\lambda_{i,H} = \lambda_{i,\mathrm{HPS}} - 25.475 + 0.14537T - 0.00020059T^2 \quad (7)$$

where i is the residue; H and A correspond to hydrophobic and aromatic residues. The λ_{HPS} is adapted from the hydropathy scale proposed by Urry *et al.*[37,53] Temperature, T is given in Kelvin throughout this paper.

When temperature dependence is included in λ_{ij}, the depth of potential well ε_{ij} is given by $\varepsilon_{ij} = \sqrt{\varepsilon_i \varepsilon_j}$ and the $\varepsilon_{ij}(T)$ is the temperature-dependent depth of the potential:

$$\varepsilon_{ij} = -0.254 + 0.00542T - 0.000006775T^2 \quad (8)$$

We have used Debye Hückel screening $U_{\mathrm{DH}}(r,i,j) = \frac{q_i \cdot q_j \exp(-\kappa \cdot r)}{4\pi D r}$, where κ^{-1} is the Debye screening length and $D = 80$ is the dielectric constant of water. In the present study, we have used two values of κ^{-1} = 1 nm and 1.92 nm corresponding to 100 mM and 25 mM salt concentration, respectively.

In the Debye–Hückel mean-field treatment, the effect of charge correlations is neglected, assuming that the ionic charges of the solution contribute to a uniform and isotropic screening field. DH potential performs well for physiological salt concentrations and is commonly used in coarse-grained models that recapitulate single chains and condensate phases of proteins.

Given the highly charged nature of polycation–RNA mixtures, we have performed additional simulations to compare the mean field DH electrostatic treatment with a more precise Particle–particle particle-mesh (PPPM) method[57,58] with no electrostatic truncation including simulations with explicit ions. We note that particle–Particle Particle-Mesh (P3M) methods go beyond the mean field approximation and consider charge correlations and longer-range forces, which can give rise to ordering not seen in mean field DH treatments. The PPPM method, as implemented in Hoomd-blue molecular dynamics library, separates the interaction between the particles into short and long-range terms, where the short-range term is calculated directly by particle–particle summation. In contrast, the long-range term is calculated by solving Poisson's equation.

The protein and RNA length and stoichiometries are adapted directly from the experimental study performed by Alsharedah *et al.*[19] Hence, the sequence length of K_4 and rU_{100} are fixed in all simulations to be 4 and 100, respectively. The protein to RNA charge ratio is fixed at $\frac{q_-}{q_+} = 1$. For each rU_{100} and K_4 mixture, we have studied the system at different non-bonded pairwise interaction potentials and employed different methods for evaluating the electrostatic term. Table 1 summarizes the potentials of all the systems studied in the present investigation.

We begin each simulation by randomly placing RNA chains and protein at a low density ($\rho = N/L^3 = 0.02$) in a periodic cubic box of 100 nm. This corresponds to 10^2 rU_{100} chains and 25×10^2 K_4 protein units.

The chain configurations are energy minimized and heated to their respective temperatures. To visualize the formation of the condensates, the production sampling is then carried out for $\sim 10^7$ steps with integration time step $\Delta t = 0.01$, during which the uncorrelated configurations are saved at intervals of $\sim 10^4$ steps. For liquid–vapor coexistence simulations, we utilize a method[59,60] in which the concentrated liquid phase is simulated in equilibrium with the dilute vapor phase and allows the determination of equilibrium density of both the phases. The direct coexistence simulations are initiated by first compressing a cubic box at a constant rate under the target temperature T' for 20 000 steps to arrive at a smaller periodic cubic box of length 20 nm and final density $\rho = 3.0$. The simulation box is expanded along the z-direction by 10–20 under T'. After the equilibration steps are complete, the simulation box has a slab of liquid condensate surrounded by coexisting saturated vapor of protein and RNA chains. The binodal of the liquid–vapor equilibrium is computed by fitting the simulated slab system density histogram along the expanded direction to the hyperbolic tangent profile.

2 Results

The polycation–RNA mixtures with chain-length asymmetry can display strong charge correlations and form complex structures not predicted by mean-field theories.[47,61–64] Therefore we begin the study by assessing the impact of different combinations of short and long-range non-bonded pairwise interaction potentials on the vapor–liquid coexistence. We first compare two widely used potentials employed in the studies of liquid–liquid phase-separation of disordered proteins; the LJ and Lambda potentials in combination with DH and PPPM electrostatics (Table 1).

In Fig. 2A and B, we compare the phase diagram of LJ, LJ + DH, and LJ + PPPM for rigid and non-rigid RNA chains, respectively. The angular harmonic term mentioned in the Methods section is not included for non-rigid RNA chains. In the absence of solvent-mediated forces, these systems naturally only display UCST (Fig. 3) behavior with condensates forming at lower temperatures and being dissolved at temperatures high enough to overcome the short- and attractive long-range interactions. Fig. 2C and D shows the phase diagram for HPS(T) + DH, HPS(T) + PPPM, HPS($\varepsilon(T)$) + DH for rigid and

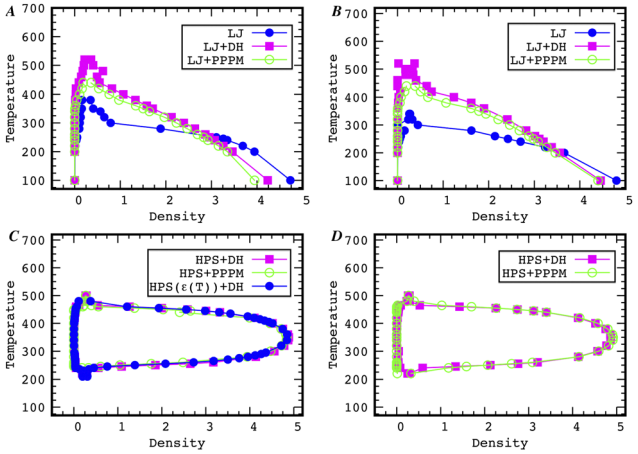

Fig. 2 Phase diagrams in the density-temperature space. LJ + DH and LJ + PPPM models are compared with (A) rigid RNA chains (B) non-rigid RNA chains. HPS + DH, HPS + PPPM, and HPS$\varepsilon(T)$ + DH models are compared with (C) rigid RNA chains (D) non-rigid RNA chains.

non-rigid RNA chains respectively. The HPS treatments effectively account for the solvent-mediated forces. Once accounting for entropic forces, the system displays UCST and LCST with condensates forming at only intermediate temperatures and dissolving at lower and higher temperatures (Fig. 3). The charged group, ε–NH_3^+ of the Lysine side chain, is charged and has hydrophobic nature, which leads to a tug of war between the penalty of desolvation and direct interactions.

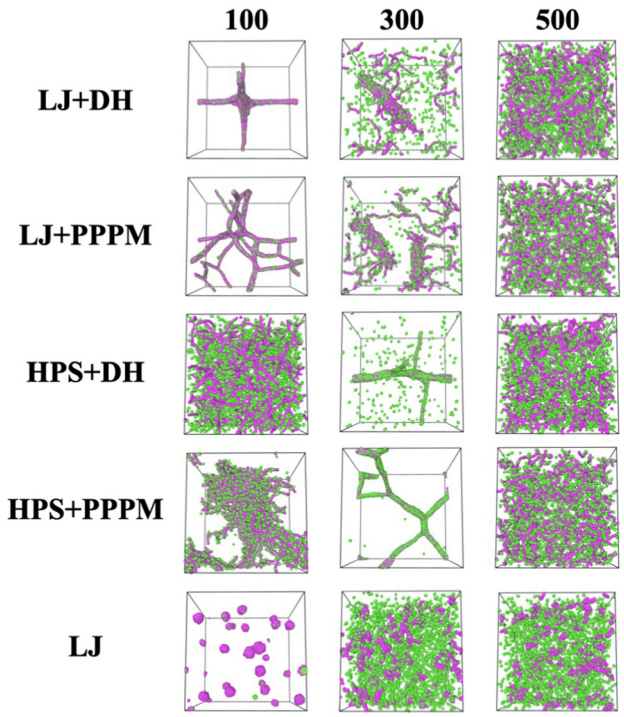

Fig. 3 *NVT* simulations of K_4 and rU_{100} in a cubic box for different residue–residue interaction pairs. Snapshots from left to right correspond to different temperatures, as indicated on the top of the image.

The condensates dissolve at low temperatures because of charge-mediated and hydrogen bonding interactions with water for lysine, and Uracyl wins over the hydrophobic interactions. At intermediate temperatures, the balance is tipped to favor desolvation, also facilitated by the formation of hydrophobic contacts.[65] As temperature increases, hydrophobic and anionic contacts eventually break, and the solution adapts well to a mixed state. This interplay of solvent and ion-mediated forces on the one hand and direct residue interactions on the other is effectively captured in our model by considering K to be a hydrophobic residue[55] in HPS(T) models and *via* temperature dependence of water dielectric constant.

Next, we examine how local chain stiffness affects structures and phase equilibrium of polycation–RNA condensates. RNA is known to form complex structures, which could be a source of additional rigidity. However, in the present study, we stay clear from sequence-encoded structural rigidity and simply account for RNA chain rigidity which can also be modulated to a significant extent by the presence of polyvalent ions.[66–68] One expects rigid chains to pay less penalty when condensing into liquid droplets than more flexible ones. We observe the phase diagrams of RNAs with rigid and nonrigid chains in the regime of an electrostatic solid are not dramatically different (Fig. 2). However, the local structures of the condensates can be dramatically affected by the local rigidity of RNA chains (Fig. 4). The condensates with rigid RNA chains are elongated and span the whole box forming a gelated architecture, whereas condensates with non-rigid RNA chains form spherical droplets. In Fig. 2A and B, we observe that in the absence of electrostatic interactions, the system unsurprisingly displays that upper critical temperature is lower because electrostatic interactions greatly assist the stability of rU_{100}–K_4 condensates.

Comparing Fig. 2A and B also shows how in the absence of electrostatic interactions, the chain rigidity affects the phase diagram. The critical point is lower when we have non-rigid chains for the LJ system; this is because rigidity aids in keeping

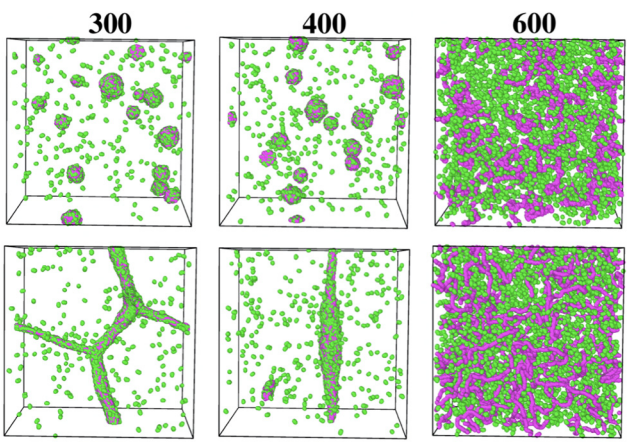

Fig. 4 Simulations of K_4–rU_{100} mixtures in Cubix box geometry for non-rigid(top) and rigid(bottom, treated with HPS + DH regime) RNA chains at different temperatures indicated at the top of the boxes.

the condensates stable by reducing the entropic penalty of restricting conformational freedom of chains.

One may also observe multi-phasic condensates in the limit where long-range electrostatic interactions are weak (see LJ in Fig. 3). For the LJ chains, condensates display layered topology with K_4 chains encapsulated by the rU_{100} chains. In Fig. 5A, we show the slab simulations comparing LJ + PPPM and LJ system at different temperatures which show the formation of multi-phasic condensates in the LJ system. The multiphasic topology of condensate in LJ treatment stems from the difference in the monomer size, which can be set *via* either the bead size or bond length of k_4 and rU_{100} chains. Thus, a mismatch in monomer size is sufficient to cause the formation of multiphasic layered topology in the absence of electrostatic interactions.

Given the highly charged nature of polycation–RNA mixtures, it is important to evaluate the differences when employing implicit *vs.* explicit treatment for electrostatic interactions. We observe that the critical temperature is slightly higher when electrostatic interactions are modeled with DH than PPPM (Fig. 2A and B). For instance, the configurations of the system treated *via* LJ + DH potential (Fig. 3), form at slightly higher densities at T = 100 K compared to the LJ + PPPM system. However, when we compare the cubic and slab simulations (Fig. 3 and 5B respectively) of systems treated *via* HPS + DH and HPS + PPPM potentials, we observe that the configurations treated *via* HPS + DH potential have a higher density.

To demystify this observation and assess which implicit ion model is closer to the explicit ion model, we compare the phase diagram at 25 mM NaCl of the explicit and implicit ion models (DH and PPPM) in Fig. 6. We have selected 25 mM NaCl concentration to reduce the computation time for the explicit ion model. To simulate the explicit ion model, we put an equal number of Na^+ and Cl^- ions in the system. We observe that

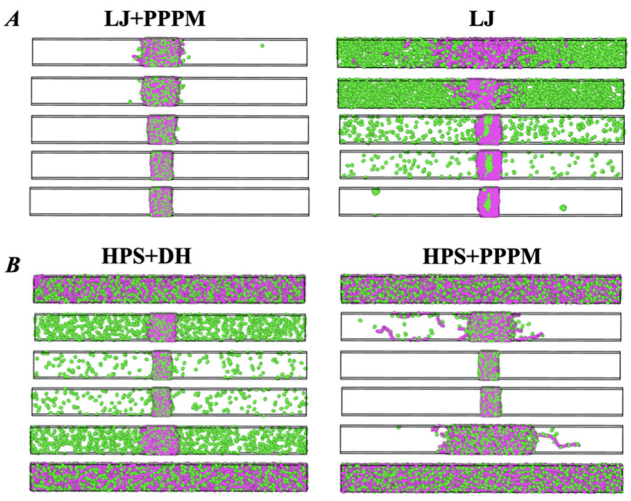

Fig. 5 Snapshots of direct coexistence simulations corresponding to Energy function treated (A) with LJ + PPPM (left) and LJ (right) potentials (B) HPS + DH (left) and HPS + PPPM (right) potentials. Temperatures have been selected to depict the formation and dissociation of the condensates for two distinct regimes modeled by the hydropathy scale and LJ potentials.

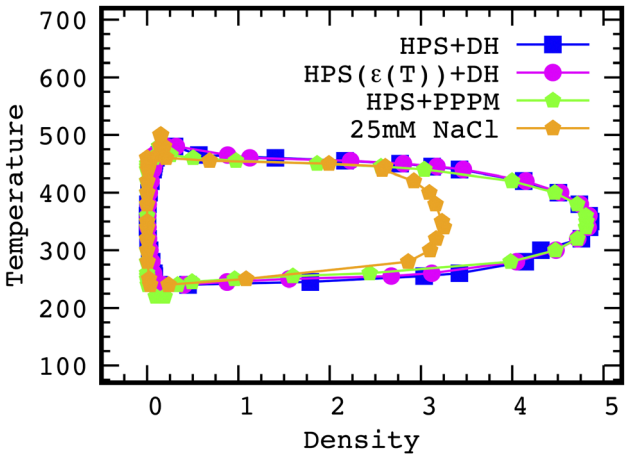

Fig. 6 Phase diagram in the density-temperature space at 25 mM NaCl of explicit ion model (25 mM NaCl) and implicit ion models (HPS + DH, HPS($\varepsilon(T)$) + DH, HPS + PPPM).

external crowding significantly reduces the density of the condensates formed in the presence of explicit ions. However, the behavior of the phase diagram looks similar to the systems where electrostatics are treated with implicit electrostatic interactions.

Finally, we compare the reduced density profiles of rU_{100} and K_4 along the z direction of the elongated simulation box at two different temperatures in Fig. 7 at 25 mM salt concentration. At T = 350 K, which is far below critical temperature the reduced density profile of rU_{100} and K_4 is identical for all three models. However, at T = 460 K which is close to the critical temperature the condensates dissolve for the explicit ion and PPPM model but do not for the DH model. This result simply confirms that PPPM electrostatics is more successful in reproducing the explicit ion behavior of condensates compared to the DH electrostatics treatment.

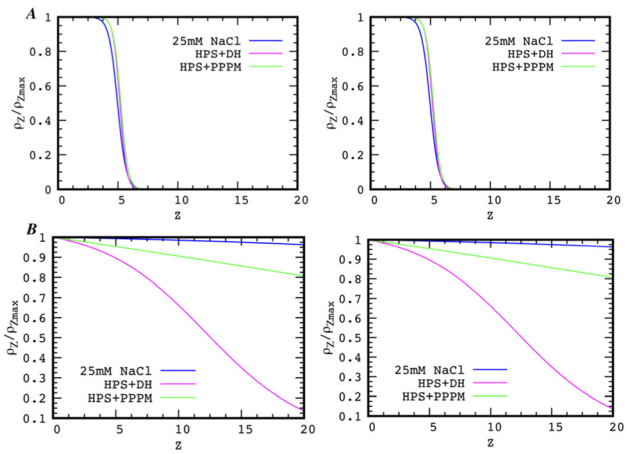

Fig. 7 Reduced density profile of rU_{100} and K_4 along the z direction of the simulation box at temperatures for 3 electrostatics treatments: explicit ions, DH, and PPPM all evaluated at 25 mM salt concentration and at two temperatures; (A) T = 350 K $< T_c$ and (B) T = 460 K $\sim T_c$.

3 Discussion

Phase-separation of biomolecules is implicated in the formation of numerous membranless compartments in cells, the functional roles of which are still poorly understood. One potential function of these compartments is to organize and regulate RNA metabolism, transcription, processing, expression, and gene silencing.[5,69] Therefore, it has become imperative to understand the driving forces and rheological characteristics of protein–RNA condensates which can shed light to functional dynamics of membraneless compartments in cells.

Recent report on the polycation peptide–RNA mixtures[19] has shown the existence of lower and upper critical solution temperatures, highlighting the signficance of temperature-dependent solvent and ion-mediated forces. In this work, we have employed molecular dynamics simulations with coarse-grained residue resolution models to dissect the contribution of temperature-dependent dielectric permittivity, and salt-induced chain swelling in modulating phase equilibrium in RNA polycation mixtures.

We find that for fitting phase diagrams to experiments, temperature-dependent solvent-mediated interactions encoded by a dielectric constant in conjunction with residue-specific coarse-grained models are sufficient. Another closely related way to account for solvent-mediated interactions is through temperature dependence of hydrophobic forces.[42] That is, when considering *Lysine* to be hydrophobic and *rU* to be aromatic[55,56] we were able to explain the experimentally observed closed-loop phase diagram where LCST < UCST using established hydrophobicity scale models.[19]

Studies of single-chain polyelectrolytes and coacervates have shown that chains' local structure significantly impacts the coexistence window.[70] Furthermore, the interplay of ions of different sizes can induce local chain rigidification or collapse, depending on the scaling regime.[64,71] Therefore we have introduced local bending potential to also study the effect of chain stiffness on the condensate topology and thermodynamic stability. We show that chain rigidity can dramatically impact the topology of condensates without changing the global phase diagram. Specifically, in the limit of weak electrostatic interactions, chain rigidity aids in keeping the condensates stable and elevates the critical temperature. In the limit of strong electrostatic interactions, chain rigidity reduces the coexistence window. Regading the topology of condensates, the flexible chains tend to form spherical droplets, whereas rigid chains percolate throughout the simulation box, forming gelated structures with large characteristic length scales. Future studies will investigate this phenomenon more quantitatively by looking at the nature of RNA-ion, RNA–RNA, and protein–RNA association with higher resolution models.

To assess the contribution of ion release and partitioning, we have compared the explicit ion model with models where electrostatic interactions are calculated by DH and PPPM methods. The global phase diagrams appear consistent for all three methods. Still, careful inspection reveals that PPPM electrostatics, where electrostatic interactions are calculated without truncating the long-range Coulomb interactions is closer to the explicit ion model than DH electrostatics in predicting the critical temperatures.

Conflicts of interest

There are no conflicts to declare.

Acknowledgements

This work was supported by funds from the National Institute of General Medical Sciences with grant no. R35 GM138243 to D.A.P.

Notes and references

1 C. P. Brangwynne, C. R. Eckmann, D. S. Courson, A. Rybarska, C. Hoege, J. Gharakhani, F. Jülicher and A. A. Hyman, *Science*, 2009, **324**, 1729–1732.
2 J. A. Ditlev, L. B. Case and M. K. Rosen, *J. Mol. Biol.*, 2018, **430**, 4666–4684.
3 P. Li, S. Banjade, H.-C. Cheng, S. Kim, B. Chen, L. Guo, M. Llaguno, J. V. Hollingsworth, D. S. King and S. F. Banani, *et al.*, *Nature*, 2012, **483**, 336–340.
4 T. J. Nott, E. Petsalaki, P. Farber, D. Jervis, E. Fussner, A. Plochowietz, T. D. Craggs, D. P. Bazett-Jones, T. Pawson and J. D. Forman-Kay, *et al.*, *Mol. Cell*, 2015, **57**, 936–947.
5 Y. Lin, D. S. Protter, M. K. Rosen and R. Parker, *Mol. Cell*, 2015, **60**, 208–219.
6 L. D. Muiznieks, S. Sharpe, R. Pomès and F. W. Keeley, *J. Mol. Biol.*, 2018, **430**, 4741–4753.
7 N. B. Nedelsky and J. P. Taylor, *Nat. Rev. Neurol.*, 2019, **15**, 272–286.
8 M. Feric, N. Vaidya, T. S. Harmon, D. M. Mitrea, L. Zhu, T. M. Richardson, R. W. Kriwacki, R. V. Pappu and C. P. Brangwynne, *Cell*, 2016, **165**, 1686–1697.
9 H. Falahati and E. Wieschaus, *Proc. Natl. Acad. Sci. U. S. A.*, 2017, **114**, 1335–1340.
10 J. A. Riback, C. D. Katanski, J. L. Kear-Scott, E. V. Pilipenko, A. E. Rojek, T. R. Sosnick and D. A. Drummond, *Cell*, 2017, **168**, 1028–1040.
11 S. Kroschwald, M. C. Munder, S. Maharana, T. M. Franzmann, D. Richter, M. Ruer, A. A. Hyman and S. Alberti, *Cell Rep.*, 2018, **23**, 3327–3339.
12 K. A. Burke, A. M. Janke, C. L. Rhine and N. L. Fawzi, *Mol. Cell*, 2015, **60**, 231–241.
13 V. H. Ryan, G. L. Dignon, G. H. Zerze, C. V. Chabata, R. Silva, A. E. Conicella, J. Amaya, K. A. Burke, J. Mittal and N. L. Fawzi, *Mol. Cell*, 2018, **69**, 465–479.
14 R. J. Stewart, C. S. Wang, I. T. Song and J. P. Jones, *Adv. Colloid Interface Sci.*, 2017, **239**, 88–96.
15 H.-X. Zhou, J.-H. Spille and P. R. Banerjee, *Phase-separated Biomolecular Condensates: Methods and Protocols*, Springer Nature, 2022.

16 W. E. Arter, R. Qi, N. A. Erkamp, G. Krainer, K. Didi, T. J. Welsh, J. Acker, J. Nixon-Abell, S. Qamar and J. Guillén-Boixet, *et al.*, *Nat. Commun.*, 2022, **13**, 7845.
17 D. Qian, T. J. Welsh, N. A. Erkamp, S. Qamar, J. Nixon-Abell, G. Krainer, P. S. George-Hyslop, T. C. Michaels and T. P. Knowles, *Phys. Rev. X*, 2022, **12**, 041038.
18 T. Kaur, M. Raju, I. Alshareedah, R. B. Davis, D. A. Potoyan and P. R. Banerjee, *Nat. Commun.*, 2021, **12**, 1–16.
19 P. Pullara, I. Alshareedah and P. R. Banerjee, *Soft Matter*, 2022, **18**, 1342–1349.
20 I. Alshareedah, T. Kaur, J. Ngo, H. Seppala, L.-A. D. Kounatse, W. Wang, M. M. Moosa and P. R. Banerjee, *J. Am. Chem. Soc.*, 2019, **141**, 14593–14602.
21 J. Wang, J.-M. Choi, A. S. Holehouse, H. O. Lee, X. Zhang, M. Jahnel, S. Maharana, R. Lemaitre, A. Pozniakovsky and D. Drechsel, *et al.*, *Cell*, 2018, **174**, 688–699.
22 R. M. Vernon, P. A. Chong, B. Tsang, T. H. Kim, A. Bah, P. Farber, H. Lin and J. D. Forman-Kay, *eLife*, 2018, **7**, e31486.
23 A. C. Murthy, G. L. Dignon, Y. Kan, G. H. Zerze, S. H. Parekh, J. Mittal and N. L. Fawzi, *Nat. Struct. Mol. Biol.*, 2019, **26**, 637–648.
24 B. S. Schuster, G. L. Dignon, W. S. Tang, F. M. Kelley, A. K. Ranganath, C. N. Jahnke, A. G. Simpkins, R. M. Regy, D. A. Hammer and M. C. Good, *et al.*, *Proc. Natl. Acad. Sci. U. S. A.*, 2020, **117**, 11421–11431.
25 Y. Yang, H. B. Jones, T. P. Dao and C. A. Castaneda, *J. Phys. Chem. B*, 2019, **123**, 3618–3629.
26 E. W. Martin, A. S. Holehouse, I. Peran, M. Farag, J. J. Incicco, A. Bremer, C. R. Grace, A. Soranno, R. V. Pappu and T. Mittag, *Science*, 2020, **367**, 694–699.
27 S. Elbaum-Garfinkle, Y. Kim, K. Szczepaniak, C. C.-H. Chen, C. R. Eckmann, S. Myong and C. P. Brangwynne, *Proc. Natl. Acad. Sci. U. S. A.*, 2015, **112**, 7189–7194.
28 S. Qamar, G. Wang, S. J. Randle, F. S. Ruggeri, J. A. Varela, J. Q. Lin, E. C. Phillips, A. Miyashita, D. Williams and F. Ströhl, *et al.*, *Cell*, 2018, **173**, 720–734.
29 G. L. Dignon, W. Zheng, R. B. Best, Y. C. Kim and J. Mittal, *Proc. Natl. Acad. Sci. U. S. A.*, 2018, **115**, 9929–9934.
30 W. Zheng, G. L. Dignon, N. Jovic, X. Xu, R. M. Regy, N. L. Fawzi, Y. C. Kim, R. B. Best and J. Mittal, *J. Phys. Chem. B*, 2020, **124**, 11671–11679.
31 R. M. Regy, G. L. Dignon, W. Zheng, Y. C. Kim and J. Mittal, *Nucleic Acids Res.*, 2020, **48**, 12593–12603.
32 J.-E. Shea, R. B. Best and J. Mittal, *Curr. Opin. Struct. Biol.*, 2021, **67**, 219–225.
33 J.-M. Choi, F. Dar and R. V. Pappu, *PLoS Comput. Biol.*, 2019, **15**, e1007028.
34 Y.-H. Lin, J. P. Brady, J. D. Forman-Kay and H. S. Chan, *New J. Phys.*, 2017, **19**, 115003.
35 U. Baul, D. Chakraborty, M. L. Mugnai, J. E. Straub and D. Thirumalai, *J. Phys. Chem. B*, 2019, **123**, 3462–3474.
36 R. Laghmach, I. Alshareedah, M. Pham, M. Raju, R. Priya and D. A. Potoyan, *et al.*, *iscience*, 2022, 104105.
37 R. M. Regy, J. Thompson, Y. C. Kim and J. Mittal, *Protein Sci.*, 2021, **30**, 1371–1379.
38 S. Das, Y.-H. Lin, R. M. Vernon, J. D. Forman-Kay and H. S. Chan, *Proc. Natl. Acad. Sci. U. S. A.*, 2020, **117**, 28795–28805.
39 G. Tesei, T. K. Schulze, R. Crehuet and K. Lindorff-Larsen, *Proc. Natl. Acad. Sci. U. S. A.*, 2021, **118**, e2111696118.
40 G. Krainer, T. J. Welsh, J. A. Joseph, J. R. Espinosa, S. Wittmann, E. de Csilléry, A. Sridhar, Z. Toprakcioglu, G. Gudiškyte and M. A. Czekalska, *et al.*, *Nat. Commun.*, 2021, **12**, 1–14.
41 J. A. Joseph, A. Reinhardt, A. Aguirre, P. Y. Chew, K. O. Russell, J. R. Espinosa, A. Garaizar and R. Collepardo-Guevara, *Nat. Comput. Sci.*, 2021, **1**, 732–743.
42 G. L. Dignon, W. Zheng, Y. C. Kim and J. Mittal, *ACS Cent. Sci.*, 2019, **5**, 821–830.
43 G. L. Dignon, R. B. Best and J. Mittal, *Annu. Rev. Phys. Chem.*, 2020, **71**, 53.
44 I. Alshareedah, M. M. Moosa, M. Pham, D. A. Potoyan and P. R. Banerjee, *Nat. Commun.*, 2021, **12**, 1–14.
45 I. Alshareedah, G. M. Thurston and P. R. Banerjee, *Biophys. J.*, 2021, **120**, 1161–1169.
46 I. Alshareedah, M. M. Moosa, M. Raju, D. A. Potoyan and P. R. Banerjee, *Proc. Natl. Acad. Sci. U.S.A.*, 2020, **117**, 15650–15658.
47 A. S. Ylitalo, C. Balzer, P. Zhang and Z.-G. Wang, *Macromolecules*, 2021, **54**, 11326–11337.
48 S. Chen and Z.-G. Wang, *Proc. Natl. Acad. Sci. U.S.A.*, 2022, **119**, e2209975119.
49 A. N. Singh and A. Yethiraj, *J. Phys. Chem. B*, 2020, **124**, 1285–1292.
50 J. Mueterthies and D. A. Potoyan, *Biomolecules*, 2021, **11**, 915.
51 Y.-H. Lin, J. Wessén, T. Pal, S. Das and H. S. Chan, *Phase-Separated Biomolecular Condensates: Methods and Protocols*, Springer, 2022, pp. 51–94.
52 H. S. Ashbaugh and H. W. Hatch, *J. Am. Chem. Soc.*, 2008, **130**, 9536–9542.
53 D. W. Urry, D. C. Gowda, T. M. Parker, C.-H. Luan, M. C. Reid, C. M. Harris, A. Pattanaik and R. D. Harris, *Biopolymers*, 1992, **32**, 1243–1250.
54 H. C. Andersen, D. Chandler and J. D. Weeks, *Adv. Chem. Phys.*, 1976, **34**, 105.
55 H. J. Dyson, P. E. Wright and H. A. Scheraga, *Proc. Natl. Acad. Sci. U. S. A.*, 2006, **103**, 13057–13061.
56 T. L. Galvão, I. M. Rocha, M. D. Ribeiro da Silva and M. A. Ribeiro da Silva, *J. Phys. Chem. A*, 2013, **117**, 5826–5836.
57 D. N. LeBard, B. G. Levine, P. Mertmann, S. A. Barr, A. Jusufi, S. Sanders, M. L. Klein and A. Z. Panagiotopoulos, *Soft Matter*, 2012, **8**, 2385–2397.
58 J. W. Eastwood, R. W. Hockney and D. Lawrence, *Comput. Phys. Commun.*, 1980, **19**, 215–261.
59 F. J. Blas, L. G. MacDowell, E. de Miguel and G. Jackson, *J. Chem. Phys.*, 2008, **129**, 144703.
60 K. S. Silmore, M. P. Howard and A. Z. Panagiotopoulos, *Mol. Phys.*, 2017, **115**, 320–327.
61 S. P. Danielsen, S. Panyukov and M. Rubinstein, *Macromolecules*, 2020, **53**, 9420–9442.

62 A. M. Rumyantsev, A. Johner, M. V. Tirrell and J. J. de Pablo, *Macromolecules*, 2022, **55**, 6260–6274.
63 S. Friedowitz, A. Salehi, R. G. Larson and J. Qin, *J. Chem. Phys.*, 2018, **149**, 163335.
64 A. M. Rumyantsev and A. Johner, *Macromolecules*, 2023, DOI: **10.1021/acs.macromol.3c00512**.
65 E. Choi and A. Yethiraj, *ACS Macro Lett.*, 2015, **4**, 799–803.
66 H. T. Nguyen, N. Hori and D. Thirumalai, *Proc. Natl. Acad. Sci. U. S. A.*, 2019, **116**, 21022–21030.
67 A. Halder, S. Kumar, O. Valsson and G. Reddy, *J. Chem. Theory Comput.*, 2020, **16**, 6702–6715.
68 V. Ramachandran, A. Mainan and S. Roy, *Phys. Chem. Chem. Phys.*, 2022, **24**, 24570–24581.
69 H. J. Wiedner and J. Giudice, *Nat. Struct. Mol. Biol.*, 2021, **28**, 465–473.
70 K. Shen and Z.-G. Wang, *Macromolecules*, 2018, **51**, 1706–1717.
71 Y. D. Gordievskaya, A. A. Gavrilov and E. Y. Kramarenko, *Soft Matter*, 2018, **14**, 1474–1481.